Imaging of *Plasmodium* Liver Stages to Drive Next-Generation Antimalarial Drug Discovery

Stephan Meister, *et al.*

Science **334**, 1372 (2011);
DOI: 10.1126/science.1211936

interlaboratory bias related to calibration of the tracer solutions used in different laboratories. Mundil *et al*. (*18*) combined recalculated ^{40}Ar-^{39}Ar dates for bed 25 from Meishan (252.1 ± 1.6 Ma) with the earlier study showing that ^{40}Ar-^{39}Ar dates of flood basalts and bed 25 are the same age (*9*) to conclude that the flood basalts and extinction are essentially synchronous. Recent work has focused on the role of large intrusions of basaltic magmas that have interacted with organic-rich shales and petroleum-bearing evaporites that may have caused large quantities of greenhouse gases to be released at 252.0 ± 0.4 Ma (*38*).

Our studies indicate that both marine and terrestrial ecosystems collapsed very suddenly, and massive release of thermogenic CO_2, as well as methane, is a highly plausible explanation (*29*, *39*). Our data on the timing and pace of the end-Permian mass extinction are consistent with rapid CO_2 increase as indicated by distinct paleophysiologic effects of the ecosystem (*15*), a sharp drop in O_2 (*40*), and substantial addition of atmospheric sulfate-bearing aerosols. These critical inputs could have resulted in increased continental aridity by rapid global warming, which caused widespread wildfires and accelerated deforestation in the world. Rapid deforestation further enhanced the continental weathering and finally resulted in a catastrophic soil erosion on the continent at PTB (*30*).

References and Notes

1. C. Q. Cao *et al*., *Earth Planet. Sci. Lett.* **281**, 188 (2009).
2. Y. Isozaki, *Science* **276**, 235 (1997).
3. G. A. Brennecka, A. D. Herrmann, T. J. Algeo, A. D. Anbar, *Proc. Natl. Acad. Sci. U.S.A.* **108**, 17631 (2011).
4. M. J. de Wit *et al*., *J. Geol.* **110**, 227 (2002).
5. Y. G. Jin *et al*., *Science* **289**, 432 (2000).
6. E. S. Krull *et al*., *Palaeogeogr. Palaeoclimatol. Palaeoecol.* **204**, 297 (2004).
7. J. L. Payne *et al*., *Science* **305**, 506 (2004).
8. S. L. Kamo *et al*., *Earth Planet. Sci. Lett.* **214**, 75 (2003).
9. P. R. Renne, M. T. Black, Z. Zichao, M. A. Richards, A. R. Basu, *Science* **269**, 1413 (1995).
10. L. Becker, R. J. Poreda, A. G. Hunt, T. E. Bunch, M. Rampino, *Science* **291**, 1530 (2001).
11. D. H. Erwin, *The Great Paleozoic Crisis: Life and Death in the Permian* (Columbia Univ. Press, New York, 1993).
12. K. Grice *et al*., *Science* **307**, 706 (2005).
13. S. C. Xie *et al*., *Geology* **35**, 1083 (2007).
14. J. L. Payne *et al*., *Geol. Soc. Am. Bull.* **119**, 771 (2007).
15. A. H. Knoll, R. K. Bambach, J. L. Payne, S. Pruss, W. W. Fischer, *Earth Planet. Sci. Lett.* **256**, 295 (2007).
16. Materials and methods are available as supporting material on *Science* Online.
17. S. A. Bowring *et al*., *Science* **280**, 1039 (1998).
18. R. Mundil, K. R. Ludwig, I. Metcalfe, P. R. Renne, *Science* **305**, 1760 (2004).
19. R. Mundil *et al*., *Earth Planet. Sci. Lett.* **187**, 131 (2001).
20. S. Z. Shen *et al*., *Palaeoworld* **15**, 3 (2006).
21. H. F. Yin, Q. L. Feng, X. L. Lai, A. Baud, J. N. Tong, *Global Planet. Change* **55**, 1 (2007).
22. C. V. Looy, R. J. Twitchett, D. L. Dilcher, J. H. Van Konijnenburg-Van Cittert, H. Visscher, *Proc. Natl. Acad. Sci. U.S.A.* **98**, 7879 (2001).
23. R. J. Twitchett, C. V. Looy, R. Morante, H. Visscher, P. B. Wignall, *Geology* **29**, 351 (2001).
24. P. D. Ward *et al*., *Science* **307**, 709 (2005).
25. Y. Q. Peng, J. X. Yu, Y. Q. Gao, F. Q. Yang, *J. Asian Earth Sci.* **28**, 291 (2006).
26. G. J. Retallack, J. J. Veevers, R. Morante, *Geol. Soc. Am. Bull.* **108**, 195 (1996).
27. W. J. Shen, Y. G. Sun, Y. T. Lin, D. H. Liu, P. X. Chai, *Geochim. Cosmochim. Acta* **75**, 1992 (2011).
28. B. M. Thomas *et al*., *Aust. J. Earth Sci.* **51**, 423 (2004).
29. S. E. Grasby, H. Sanei, B. Beauchamp, *Nat. Geosci.* **4**, 104 (2011).
30. M. A. Sephton *et al*., *Geology* **33**, 941 (2005).
31. H. Visscher, M. A. Sephton, C. V. Looy, *Geology* **39**, 883 (2011).
32. A. Riccardi, L. R. Kump, M. A. Arthur, S. D'Hondt, *Palaeogeogr. Palaeoclimatol. Palaeoecol.* **248**, 73 (2007).
33. T. J. Algeo, Z. Q. Chen, M. L. Fraiser, R. J. Twitchett, *Palaeogeogr. Palaeoclimatol. Palaeoecol.* **308**, 1 (2011).
34. B. Nabbefeld, K. Grice, R. E. Summons, L. E. Hays, C. Q. Cao, *Appl. Geochem.* **25**, 1374 (2010).
35. A. V. Milkov, *Earth Sci. Rev.* **66**, 183 (2004).
36. W. T. Holser, M. Schidlowski, F. T. Mackenzie, J. B. Maynard, in *Chemical Cycles in the Evolution of the Earth*, C. B. Gregor, R. M. Garrels, F. T. Mackenzie, J. B. Maynard, Eds. (Wiley, New York, 1988), pp. 105–173.
37. D. H. Erwin, *Extinction* (Princeton Univ. Press, Princeton, NJ (2005).
38. H. Svensen *et al*., *Earth Planet. Sci. Lett.* **277**, 490 (2009).
39. G. J. Retallack, A. H. Jahren, *J. Geol.* **116**, 1 (2008).
40. R. B. Huey, P. D. Ward, *Science* **308**, 398 (2005).

Acknowledgments: This research was supported by National Natural Science Foundation of China, the National Basic Research Program of China (2006CB806400, 2011CB808905), the Chinese Academy of Sciences (CAS)/State Administration of Foreign Experts Affairs of China (SAFEA) International Partnership Program, and CAS grants KZCX2-YW-Q08-4 and BK2010022 of the basic research program of Jiangsu Province for the Nanjing Group. Further support was provided by a U.S. National Aeronautics and Space Administration (NASA) Astrobiology Institute Grant (to S.A.B. and D.H.E.), NASA Exobiology Program grant NNX09AM88G (to C.Q.C.), NASA grant NNA08CN84A (to D.H.R.), and a Discovery Grant of the Natural Sciences and Engineering Research Council of Canada (NSERC) (to C.M.H.). All data are available in the supporting online material.

Author contributions: This paper is dedicated to Prof. Y. G. Jin, who initiated the China-U.S. joint research with S.A.B. and D.H.E. S.A.B., D.H.E., S.Z.S., and Y.W. wrote the paper with inputs from J.L.C., C.M.H., D.H.R., and P.M.S. All geochronologic ages were produced by S.A.B. and J.L.C. Diversity pattern analysis using CONOP was carried out by Y.W. and P.M.S. with the database established by Y.W. and S.Z.S. Biostratigraphy was analyzed by S.Z.S., C.M.H., and Y.W. Carbon isotope dynamic model based on the Meishan section was conducted by D.H.R. with the data from C.Q.C. All data from the terrestrial and transitional sections were analyzed by S.Z.S. and other coauthors of the Nanjing group. All authors joined in field work and contributed to the interpretation of the data.

Supporting Online Material

www.sciencemag.org/cgi/content/full/science.1213454/DC1
Materials and Methods
SOM Text
Figs. S1 to S12
Tables S1 to S4
References (*41*–*111*)

1 September 2011; accepted 28 October 2011
Published online 17 November 2011;
10.1126/science.1213454

Imaging of *Plasmodium* Liver Stages to Drive Next-Generation Antimalarial Drug Discovery

Stephan Meister,[1]* David M. Plouffe,[2]* Kelli L. Kuhen,[2] Ghislain M. C. Bonamy,[2] Tao Wu,[2]† S. Whitney Barnes,[2] Selina E. Bopp,[1] Rachel Borboa,[2] A. Taylor Bright,[1,3] Jianwei Che,[2] Steve Cohen,[2] Neekesh V. Dharia,[1] Kerstin Gagaring,[2] Montip Gettayacamin,[4] Perry Gordon,[2] Todd Groessl,[2] Nobutaka Kato,[2] Marcus C. S. Lee,[5] Case W. McNamara,[2] David A. Fidock,[5,6] Advait Nagle,[2] Tae-gyu Nam,[7]‡ Wendy Richmond,[2] Jason Roland,[2] Matthias Rottmann,[8,9] Bin Zhou,[2] Patrick Froissard,[10,11] Richard J. Glynne,[2] Dominique Mazier,[10,11,12] Jetsumon Sattabongkot,[13] Peter G. Schultz,[7] Tove Tuntland,[2] John R. Walker,[2] Yingyao Zhou,[2] Arnab Chatterjee,[2] Thierry T. Diagana,[14] Elizabeth A. Winzeler[1,2]§

Most malaria drug development focuses on parasite stages detected in red blood cells, even though, to achieve eradication, next-generation drugs active against both erythrocytic and exo-erythrocytic forms would be preferable. We applied a multifactorial approach to a set of >4000 commercially available compounds with previously demonstrated blood-stage activity (median inhibitory concentration < 1 micromolar) and identified chemical scaffolds with potent activity against both forms. From this screen, we identified an imidazolopiperazine scaffold series that was highly enriched among compounds active against *Plasmodium* liver stages. The orally bioavailable lead imidazolopiperazine confers complete causal prophylactic protection (15 milligrams/kilogram) in rodent models of malaria and shows potent in vivo blood-stage therapeutic activity. The open-source chemical tools resulting from our effort provide starting points for future drug discovery programs, as well as opportunities for researchers to investigate the biology of exo-erythrocytic forms.

Malaria continues to present a major health challenge in many of the poorest countries in the world, with 225 million cases leading to an estimated 781,000 deaths in 2009 (*1*). In humans, malaria is caused by *Plasmodium falciparum*, *P. malariae*, *P. ovale*, *P. vivax*, and the simian parasite *P. knowlesi* (*2*). *Plasmodium* is naturally transmitted by the bite of an infected female *Anopheles* mosquito. During the bite, the sporozoites are injected with the mosquito's saliva and find their way to the host liver. There the parasites multiply asexually as exo-erythrocytic forms (EEFs) during an asymptomatic incubation period of ~1 week

before emerging into the blood stream. This initiates the asexual erythrocytic cycle that is responsible for disease manifestations. Whereas the EEFs of some *Plasmodium* species have a limited life span, in the case of *P. ovale* and *P. vivax* the parasite can persist within the liver as dormant hypnozoite for several months to years (*3*). Upon hypnozoite reactivation via an unknown mechanism, parasites can repopulate the blood with rapidly multiplying parasites that can cause pathology. As a consequence, the persistence of hypnozoites represents a formidable barrier to the eradication of malaria.

The only drugs with substantial activity against proliferating EEFs and hypnozoites are the 8-aminoquinolines, including primaquine, pamaquine, and tafenoquine (*4*, *5*). Primaquine is the only treatment recommended by the World Health Organization (WHO) to eliminate liver stages (*4*). However, 8-aminoquinolines can all cause dangerous levels of methemoglobinemia as a side effect in patients with glucose-6-phosphate dehydrogenase deficiency (*6*, *7*), a common adaptive genetic condition in malaria-endemic regions. Resistance to this chemical class has also been reported, further increasing the need to find alternative drugs (*8*).

To identify leads with liver-stage activity, we refined an in vitro assay with *P. yoelii* sporozoites and HepG2-A16-CD81^{EGFP} (where EGFP indicates enhanced green fluorescent protein) cells (*9*) to screen a library of compounds known to be active against *P. falciparum* blood stages. The data revealed substantial differences in activity between blood and liver stages of the parasite and identified a chemically diverse group of molecules active against both.

Measuring sporozoite infection ratios and schizont size with high-content imaging. Only 1% of liver cells typically become infected by sporozoites in vitro, and, because we needed to

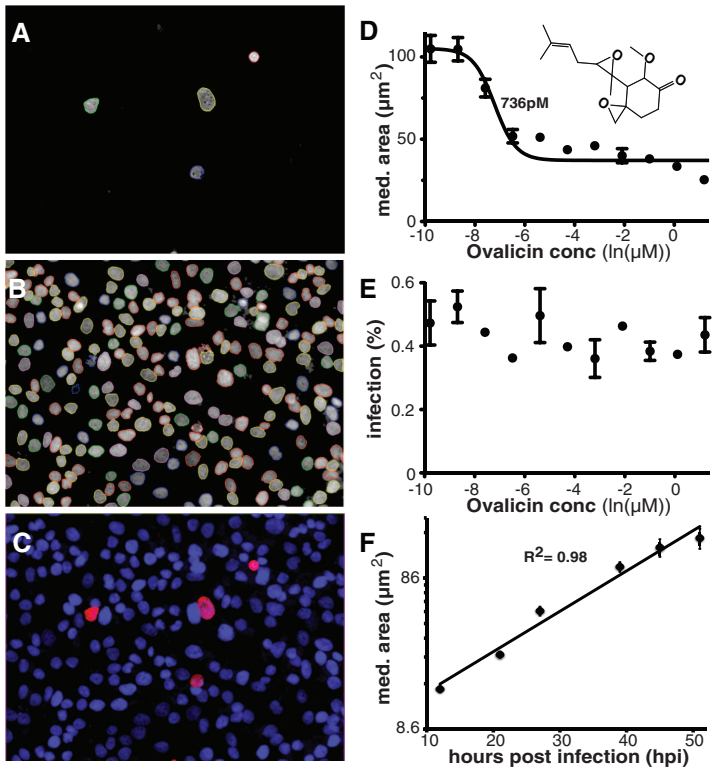

Fig. 1. Images of high-content screening of parasite hepatic schizonts and parasite growth dynamics. (**A**) *P. yoelii* sporozoites were stained 48 hours post infection (hpi) with α*Py*HSP70 antibodies. The parasites areas were defined by outlines generated by a custom Acapella script, indicating separate objects. (**B**) Hoechst 33342 nuclear staining of HepG2-A16-CD81^{EGFP} cells. Nuclei are delineated by using a script as in (A). (**C**) False-color channel merge of (A) and (B). (**D** and **E**) Measuring inhibition using parasite area. The IC_{50} of ovalicin is 736 pM when measured by median parasite area (D), but no drug effect is seen when the overall infection ratio is measured in (E). (**F**) Correlation of incubation time and schizont size. *P. yoelii* EEF growth approximates a linear rate with an R^2 of 0.98 in the HepG2-A16-CD81^{EGFP} cell line when no test compounds are added. Data are mean ± SD based on four experimental replicates of ~50 infected cells per time point.

Table 1. Blood-stage and liver-stage (EEF) IC_{50} values (with standard deviations) of select characterized compounds. Blood-stage IC_{50} values were measured against *P. falciparum* W2 parasites by using a SYBR green assay (*30*). The median EEF *P. yoelii* parasite area (in μm^2 ± SD) was calculated from two or more independent experiments with ~50 schizonts each. All drugs were dissolved in DMSO. Median parasite size of control *P. yoelii* DMSO-treated EEFs ranged from 160 to 180 μm^2. HepG2-A16-CD81^{EGFP} inhibition in the third column was calculated by determining the dose response for host nuclei number. Chloroquine was the only compound dissolved in water instead of DMSO. Maximum concentration of strobilurin tested was 1 μM. na, not applicable.

Compound	*P. yoelii* EEF IC_{50} (nM)	HepG2 inhibition IC_{50} (μM)	Median parasite area (μm^2)		Blood IC_{50} (nM)
			1 μM	10 μM	
Cyclosporin	71 ± 3	2.3 ± 0.7	<9	<9	345 ± 116
Lasalocid	37 ± 20	3.9 ± 1.4	<9	<9	50 ± 8
Pyrimethamine	2.4 ± 1.6	6.3 ± 3.3	31.1 ± 0.7	29.6 ± 2.0	15 ± 2
Berberine	224 ± 152	2.6 ± 0.5	46.4 ± 7.0	22.4 ± 2.3	117 ± 9
Atovaquone	9.4 ± 15	9.5 ± 2.5	18.2 ± 1.0	18.6 ± 1.0	2.2 ± 0.4
Primaquine	1162 ± 85	6.1 ± 1.9	56.8 ± 15.6	<9	317 ± 60
Chloroquine	1650 ± 132	1.6 ± 0.3	65.4 ± 9.5	<9	84 ± 3
Ovalicin	0.7 ± 0.3	>10	35.1 ± 3.1	19.1 ± 0.9	>10,000
Artemisinin	>10,000	>10	na	na	3.3 ± 0.4
Mefloquine	3270 ± 840	3.1 ± 0.6	65.4 ± 4.7	<9	9.5 ± 10
Strobilurin	8.8 ± 0.6	>1	22.3 ± 3	na	7 ± 0.1
Cycloheximide	78 ± 28	0.22 ± 0.10	<9	<9	366 ± 69
Decoquinate	0.16 ± 0.02	>10	17.7 ± 0.3	18.8 ± 4.7	0.25 ± 0.06

[1]Department of Genetics, The Scripps Research Institute, La Jolla, CA 92037, USA. [2]Genomics Institute of the Novartis Research Foundation, San Diego, CA 92121, USA. [3]Biomedical Sciences Graduate Program, University of California San Diego, La Jolla, CA 92093, USA. [4]Department of Veterinary Medicine, Armed Forces Research Institute of Medical Sciences (AFRIMS), Bangkok 10400, Thailand. [5]Department of Microbiology and Immunology, Columbia University Medical Center, New York, NY 10032, USA. [6]Department of Medicine (Division of Infectious Diseases), Columbia University Medical Center, New York, NY 10032, USA. [7]Department of Chemistry, The Scripps Research Institute, La Jolla, CA 92037, USA. [8]Parasite Chemotherapy, Swiss Tropical and Public Health Institute, CH-4002 Basel, Switzerland. [9]University of Basel, CH-4003 Basel, Switzerland. [10]INSERM, U945, Paris, France. [11]Université Pierre et Marie Curie–Paris (UPMC), UMR S 945 Paris, France. [12]Assistance Publique–Hôpitaux de Paris, Groupe hospitalier Pitié-Salpêtrière, Service Parasitologie-Mycologie, Paris, France. [13]Entomology Department, AFRIMS, Bangkok 10400, Thailand. [14]Novartis Institutes for Tropical Disease, Singapore.

*These authors contributed equally to this work.
†Present address: Life Technologies, 5781 Van Allen Way, Carlsbad, CA 92008, USA.
‡Present address: Gyeonggi Bio-Center, Suwon, Gyeonggi-do 443-270, Korea and College of Pharmacy, Hanyang University, Ansan, Gyeonggi-do 426-791, Korea.
§To whom correspondence may be addressed. E-mail: winzeler@scripps.edu or ewinzele@gnf.org

screen many thousands of compounds, we created a robust, reproducible assay and image analysis to automate data collection. Eight thousand sporozoites freshly dissected from infected *Anopheles stephensi* mosquitoes were added to each well of a 384-well plate, containing ~15,000 hepatoma cells per well. After a 2-day incubation in the presence of compound, the host cell and parasite nuclei were labeled with Hoechst 33342, and the parasites were labeled with α*Py*HSP70 antibodies. A PerkinElmer (Waltham, MA) high-content imaging system captured 25 images (Fig. 1) for each well of the 384-well plate. A custom Acapella (PerkinElmer) script parameterized for this assay was used to analyze the images on the basis of morphology and fluorescence intensity for each liver cell nucleus and each parasite. The infection ratio was the ratio of parasite number (α*Py*HSP70-positive) to the number of host nuclei per well.

To quantify the effects of the test compounds, we determined median parasite size to be preferable to the infection ratio, because infection ratio may be affected by drug toxicity to host cells and host cell division during the incubation (e.g., a 1% infection ratio may drop to 0.3 to 0.6% after 48 hours of exposure to a cell-toxic compound). Measuring parasite size also enabled the identification of compounds that arrest parasite growth without reducing the infection ratio. For example, the compound ovalicin reduced schizont size (Fig. 1D) with a median inhibitory concentration (IC_{50}) of 736 pM but had no measurable effect on the infection ratio (Fig. 1E). Lastly, measuring parasite size allowed us to estimate when a particular compound affected parasite development (Fig. 1F).

Performance of control compounds. For evaluation, the assay was first conducted on a set of control compounds, which confirmed that compounds known to affect only blood stages were either inactive [artemisinin and the spiroindolone, NITD609 (*10*)] or had only marginal activity (mefloquine and chloroquine) against EEFs. Other compounds with known activity against EEFs, including ovalicin, berberine, atovaquone, lasalocid, pyrimethamine, and primaquine, were confirmed as active in our assay (Table 1). The control compounds were further classified on the basis of their time of action by using schizont size, which is proportional to developmental stage and which ranged from 9 μm^2 (the smallest size detected by our imaging software and objective) up to 180 μm^2 for a fully developed untreated schizont (Fig. 1F). Because of the resolution of the microscope (~0.43 μm^2 per pixels), we could not distinguish between compounds that prevent sporozoite infection and those that arrest schizont growth at a size less than 9 μm^2 (a value too close to the average background staining). To examine this possibility, we infected and examined cultured liver cells by using deconvolution microscopy after 48 hours in the presence of drugs (fig. S1). Our results showed that liver schizonts formed at the expected rate but were very small compared with those of untreated or artemisinin-treated parasites.

We screened a set of antimalarials derived from a collection of commercially available compounds that had previously been tested for activity against blood-stage *P. falciparum* parasites (*11*, *12*). Chemical scaffold analysis based on chemical fingerprint similarities (*13*) revealed that the library of 5697 compounds was composed of 2715 independent chemical scaffold clusters, some of which were unique to this library and some of which were also hits in independent screens (fig. S2). Of the 5697 compounds, 275 could be confirmed as active against liver-stage parasites (fitted IC_{50} < 10 μM) in two rounds of screening (table S1). Two hundred twenty-nine compounds had an IC_{50} of less than 1 μM and 86 less than 100 nM.

Scaffold clustering. A major challenge associated with translating compounds into drugs is in determining which of the leads are the most promising for further medicinal chemistry development aimed at increasing a compound's exposure, physicochemical properties, and potency. The data set of 275 active compounds contains scaffolds that are distinct from known antimalarial pharmacophores (quinolines, quinones, and trioxanes) and reactive functional groups (such as Michael acceptors or nitroarenes). Such filtering still gives more leads than can be reasonably investigated, but the advantage of completing such a large screen of putative antimalarials is that it allows for a system-wide analysis of the data by exploring structure-activity relationships (SAR)

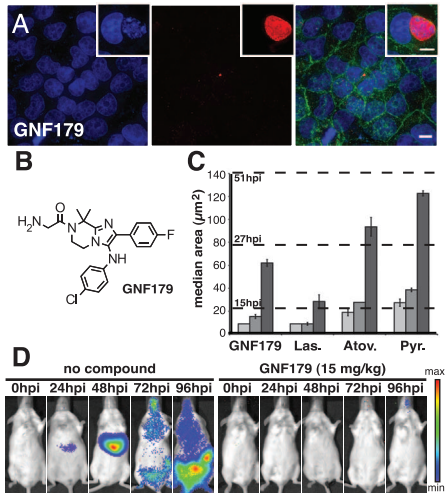

Fig. 2. The effect of GNF179 on the liver-stage parasite and comparison with lasalocid, pyrimethamine, and atovaquone. (**A**) High-resolution deconvolution microscopy of the GNF179-treated liver-stage parasites. Columns show Hoechst 33342 staining in blue, α*Py*HSP70 staining in red, and a merge with the host plasma membrane marker CD81-GFP in green. Cultures were treated with 1 μM GNF179 for 48 hours. (Insets) DMSO-treated control parasite at the same scale and time point. Scale bar indicates 10 μm. (**B**) Chemical structure of GNF179. (**C**) The targets of GNF179 and lasalocid appear to be required throughout development. Compounds were added at 1 μM final concentration at the start (lightest shade), 15 hpi (medium shade), and 27 hpi (darkest shade); all samples were incubated up to an end point of 51 hpi. Dashed lines represent the control dimethyl sulfoxide (DMSO)–treated growth levels at 15, 27, and 51 hpi. Data are mean ± SD from two experimental replicates of ~50 infected cells per time point. Las, lasalocid; Pyr, pyrimethamine; Atov, atovaquone. (**D**) In vivo bioluminescence imaging of representative mice infected with *P. berghei* and treated with GNF179 (15 mg/kg) or vehicle (no compound) at 6 hpi. In the control, luminescence showing the developing parasite was detected in the liver area from 24 hpi and the lung and gastrointestinal track region from 72 hpi. No luminescence signal was detected from GNF179 or atovaquone (2.5 mg/kg)-treated mice even at the maximum sensitivity setting, and no blood-stage parasitemia was detected from later blood smear examinations. The luminescence intensity color-coding does not represent absolute values and is individually adjusted for each recording, which is why you can see background signal around the muzzle in some of the control pictures.

Table 2. Prophylaxis testing results with *P. berghei*. The prepatent period was the average of days for all five mice tested per group. In all cases, the drug was administered orally 1 to 3 hours before sporozoite injection, except where indicated by an asterisk, where drug administration was 6 hours after infection. All dosing was in a suspension formulation of 0.5% w/v methylcellulose, 1% (v/v) solutol HS15. Dash entries, suspension formulation only; na, not applicable because of lack of blood-stage infection.

	Dose mg/kg	Average survival (%)	Prepatent period (days)
Untreated	–	0	4
Untreated*	–	0	5.3
GNF179	5 p.o.	20	4.2
GNF179	15 p.o.	100	na
GNF179*	15 p.o.	80	6.2
GNF179	20 p.o.	100	na
Atovaquone	2.5 p.o.	100	na
Atovaquone*	2.5 p.o.	100	na
NITD609	30 p.o.	0	4.2
NITD609	15 p.o.	0	4.5

within the compound library. SARs are more important than absolute potency because they indicate a chemical space that can be optimized to compounds with the desired potency (*13*).

To identify which of the 2715 scaffold clusters in the compound library would offer the most promising leads for liver-stage drugs, we identified the statistically enriched clusters composed of the 655 primary liver hits [compounds causing >50% parasite growth inhibition at 10 μM (table S2)] by using an accumulative hypergeometric mean function (HMF). This identified 62 primary clusters by using a cutoff of $P < 0.05$ (table S3) that were over- or underrepresented in the liver-stage hits. For example, the quinazolinone scaffold (cluster 2691) has 68 related members within the entire library, and only 2 of the 68 screened appeared as initial hits in the liver-stage screen (HMF $P = 9.8 \times 10^{-4}$), indicating that a compound developed from this series would be unlikely to provide causal prophylactic activity. By contrast, there were 10 members of the pyrazolopyrimidine scaffold (cluster 1766, figs. S3 and S2B and table S4), 9 of which showed initial activity in the liver assay (HMF $P = 2.8 \times 10^{-7}$). Five of the nine compounds in cluster 1766 were reconfirmed to have activity on EEFs (HMF $P = 5.1 \times 10^{-4}$), as were seven of the quinazoline scaffold (cluster 2620, HMF $P = 41.5 \times 10^{-6}$). In addition, three of the nine scaffolds containing an atovaquone-like napthoquinone core (cluster 2037, HMF $P = 3.0 \times 10^{-2}$) (fig. S3) inhibited parasite development at very early stages (12.5 to 21 μm^2). Similarly, early parasite development was inhibited by 14 compounds (cluster 2714, fig. S3) predicted to inhibit dihydrofolate reductase (DHFR) on the basis of their similarity to known DHFR inhibitors and less than one-tenth activity against Dd2, a strain that carries three point mutations in DHFR (*14*, *15*). In this cluster, 13 of the 14 were active in the initial assay (HMF $P = 2.0 \times 10^{-7}$), and all 13 showed dose-response activity, yielding very similarly sized schizonts with a median area of 24 ± 2.8 μm^2 (table S1).

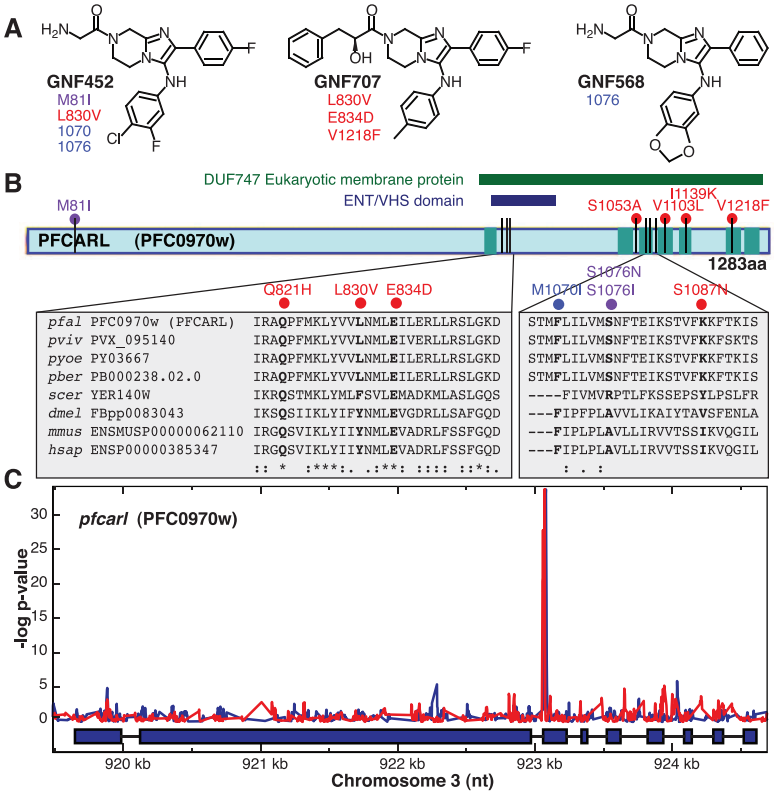

Fig. 3. SNPs identified in *pfcarl* by microarray analysis and whole-genome sequencing analysis. (**A**) Stereochemical structures of three compounds, GNF452 (B1, B2, and B3), GNF707 (C1, C2, and C3), and Pf-5069 (A1 and A2), from the IP series (table S5) used to generate resistant parasite clones. Detected SNPs, indicated below the compound IDs, are detailed in table S11 (SNPs identified by sequencing analysis are red, and SNPs identified by both sequencing and microarray analysis are purple). (**B**) Schematic of *pfcarl* showing the conserved regions, including the transmembrane domains. SNP color-coding is the same as in (A). Two regions of the protein are enlarged to show close SNPs and the amino acid sequence conservation of the region across parasite and other species (pfal, *P. falciparum*; pviv, *P. vivax*; pyoe, *P. yoelii*; pber, *P. berghei*; scer, *S. cerevisiae*; dmel, *Drosophila melanogaster*; mmus, *Mus musculus*; hsap, *Homo sapiens*). Single-letter abbreviations for the amino acid residues are as follows: A, Ala; C, Cys; D, Asp; E, Glu; F, Phe; G, Gly; H, His; I, Ile; K, Lys; L, Leu; M, Met; N, Asn; P, Pro; Q, Gln; R, Arg; S, Ser; T, Thr; V, Val; W, Trp; and Y, Tyr. (**C**) Microarray SNP analysis across *pfcarl* from two GNF452-resistant clones (GNF452-1 in blue and GNF452-3 in red). The lines trace the *P* values indicating whether mapped probes are different in the resistant clone compared with the Dd2 parental strain.

A drug candidate with liver-stage activity. Although smaller compound clusters are less impressive, they nevertheless provide interesting starting points for medicinal chemistry efforts. The imidazolopiperazine (IP) cluster 1035 is a scaffold class of saturated cyclic amines with a predicted high probability of activity against both liver- and blood-stage parasites (fig. S3 and table S5). All three members of the original data set (Pf-5069, Pf-5179, and Pf-5466) share the same IP saturated cyclic amine chemical core and showed activity in the *P. yoelii* liver assay (HMF $P = 0.0035$). These compounds also showed submicromolar IC_{50} values against *P. falciparum* blood-stage cultures in vitro, including the multidrug-resistant strain W2. The IP scaffold is attractive as a starting point for medicinal chemistry because it is structurally unrelated to known antimalarial scaffolds and is chemically tractable. In addition, it showed no cross resistance with strains having mutations that make them resistant to drugs acting on liver stages, including atovaquone (table S6) and pyrimethamine.

To test whether the modified IP scaffolds retained activity against liver-stage parasites, we examined several analogs optimized for blood-stage potency (*16*) in our *P. yoelii* liver-stage assay. As expected, all compounds in the series caused the parasites to arrest near the minimal detectable size (<9 μm^2) in the liver assay (table S5). In addition, members of the series displayed liver-stage activity that correlated well with their activity against *P. falciparum* blood stages. For example, the IC_{50}s for Pf-5069 were 454 and 334 nM against the blood stages of strains 3D7 and W2 and 221 nM in the *P. yoelii* assay using HepG2-A16-CD81^{EGFP} cells (*17*), whereas the IC_{50} values for GNF180 in the same assays were 37, 39, and 59 nM.

By synthesizing over 1200 analogs and optimizing their blood stage potency (*16*), we created derivatives of the IP lead compounds with suitable properties for testing in animal models of malaria. This work led to the design of an optimized 8,8-dimethyl IP analog (GNF179; Fig. 2, A and B; synthesis described in Materials and Methods) that exhibited the potency [4.8 nM against the multidrug-resistant strain W2 (table S5)], in vitro metabolic stability, and in vivo oral bioavailability (58%) required for an antimalarial drug development candidate (table S7). GNF179 exhibits a low clearance ($CL = 22$ ml/min per kg, ~25% of hepatic blood flow in mice), a large volume of distribution (steady-state volume of distribution, $V_{ss} = 11.8$ l/kg), a mean residence time (MRT = 9 hours), and suitable terminal half-life ($t_{1/2} = 8.9$ hours). As expected for a compound with potency in the low nanomolar range and good pharmacokinetic properties, GNF179 reduced *P. berghei* parasitemia levels by 99.7% with a single 100 mg/kg oral dose and prolonged mouse survival by an average of

19 days. In contrast, we found that the average survival times for chloroquine and artesunate in mice infected with *P. berghei* and given a single oral dose at 100 mg/kg were 12.5 and 7 days, respectively (table S8). To demonstrate that the compound was suitable for testing for causal prophylactic activity, we confirmed that the compound was distributed into the liver. On oral dosing, we found a maximum concentration (C_{max}) within the liver of 55 μM at 15 mg/kg and 193 μM at 100 mg/kg, with a half-life of 7 to 9 hours, similar to that in plasma (table S9). The overall oral exposure (area under the curve) liver-to-plasma ratios of 55 and 25 at the 15 and 100 mg/kg oral administration (p.o.) doses, respectively, further confirm good liver exposure to the compound.

GNF179 works through a distinct mechanism. To confirm in vivo the tissue schizonticidal activity observed in vitro, we tested GNF179 in a rodent malaria model of causal prophylactic treatment (Table 2). Groups of five mice were given a single dose of atovaquone (positive control), GNF179, or the negative control NITD609 (*10*) and then injected with 10^5 *P. berghei* sporozoites. Although NITD609 is slightly more potent against *P. falciparum* blood stages than GNF179 (~1 nM versus 7 nM) and is fully curative at a 100 mg/kg oral dose in a blood-stage animal model (*10*), GNF179 was able to protect against an infectious *P. berghei* sporozoite challenge with a single oral dose at 15 mg/kg (Fig. 2D), whereas NITD609 was not (Table 2). Taken together, these data show that the in vitro HepG2-A16-CD81^{EGFP} assay correlates well with in vivo efficacy and that compounds identified in this cellular screening approach offer evidence of causal prophylactic activity.

Examination of infected cells treated with GNF179 by high-resolution microscopy showed that this compound series causes the parasites to arrest at the earliest stages of development (Fig. 2, A and C), even earlier than atovaquone and the antifolates. Because IP compounds may act only during a short period of early development, the efficacy of compounds given 15 and 27 hours postinvasion was tested. These data showed that, when pyrimethamine was added 27 hours postinvasion, the parasites grew to normal size (Fig. 2C), indicating that folates are needed only at a specific time in development. In contrast, GNF179, like lasalocid and atovaquone, remained active later in EEF development, and the rapidly induced growth arrest could not be reversed after compound removal. GNF179 may act against sporozoites instead of hepatic stages; thus, the compound was also administered to mice 6 hours after infection. Luciferase imaging showed that no blood stage infection developed (Fig. 2D and Table 2), indicating that the target of GNF179 is needed for continuous growth and development of the parasite in the liver.

Unlike other compounds that act early in hepatic stage development, such as cycloheximide, GNF179 does not rapidly inhibit parasite protein biosynthesis (fig. S4); nor is it likely to target parasite cytochrome bc_1, which has been validated as a hepatic stage target for atovaquone, because we see no cross resistance (table S6). In addition, unlike electron chain transport inhibitors, members of the IP scaffold do not cause a shift in IC_{50} when tested against transgenic parasites lines expressing *Saccharomyces cerevisiae* dihydroorotate dehydrogenase (table S10) (*18*, *19*). To confirm that the mechanism of action was distinct, we exposed *P. falciparum* Dd2 and 3D7 parasite strains to increasing concentrations of the IP series (GNF452, GNF707, and Pf-5069) until resistance emerged (Fig. 3A). Mutants were cloned, and the genomes of the resistant clones were compared with the parental parasites by using high-density microarrays or full genome sequencing (table S11 and Fig. 3B). The mutants showed no cross resistance (i.e., no changes in IC_{50}) for mefloquine (~16 nM) or artemisinin (~6 nM). Microarray analysis revealed only between one and six high-probability genetic changes per mutant genome (Fig. 3 and tables S11 and S12). Notably, only a single gene (PFC0970w), which we have named *P. falciparum* cyclic amine resistance locus (*pfcarl*), encoding an uncharacterized protein with seven predicted transmembrane regions, was mutated in all strains. We observed no new genetic changes [either single nucleotide polymorphisms (SNPs) or copy number variations (CNVs)] in *pfmdr1*, *pfcrt*, or any other known *Plasmodium* drug-resistance gene. Full-genome sequencing of four of the independently derived drug-resistant clones showed six high-quality SNPs that distinguished the drug-pressured parasites from the parental Dd2 clone. Five of those SNPs were in *pfcarl*. Additional selection of Dd2 parasites with related scaffolds produced three resistant clones (D1, D2, and D3), which each harbored a single nonsynonymous point mutation in *pfcarl* (table S11).

Homologs of *pfcarl* are conserved across almost all eukaryotic genera, including humans [OrthoMCL group summary (OG4_11754)], and the homolog is essential in *Caenorhabditis elegans* (*20*). Analysis of the corresponding yeast deletion strains (*21*) suggests that the gene plays a role in protein folding within the endoplasmic reticulum (*22*), a process that in *Plasmodium* would presumably be required in both blood and hepatic stages. All mutations observed in our resistant clones affected amino acids that were evolutionarily conserved. Polymorphism data across various different strains in *P. falciparum* (*23*) also indicate conservation. Although more work is needed to characterize this gene, our data suggest that the IPs have a mechanism of action distinct from known antimalarials and that *pfcarl* could represent a conserved drug target or resistance gene.

Dual-stage antimalarial drug development. Recent efforts to develop novel malaria control measures recognize that ideally antimalarials should be active against liver stages as well as blood stages (*24*). Compounds with dual activity are rare among the antimalarials that are licensed or in development. Indeed, tests with compounds in clinical development, including OZ277 (*25*) and OZ439 (*26*), showed that, whereas most are equally potent against blood stages, only atovaquone and the antifolates showed equivalent potency to GNF179 in the HepG2-A16-CD81^{EGFP} model. It is also worth noting that compounds related to naphthoquinones (cluster 2037) and DHFR inhibitors (cluster 2714) were identified in a previously reported in vivo screening effort aimed at identifying liver-stage antimalarial drugs using whole animal testing (*27*). Our data set reveals compounds that could offer starting points for the development of dual-stage antimalarial drugs.

One outstanding question is whether these scaffolds can also provide radical cure activity against the dormant liver stages of the *P. vivax* parasite. To our knowledge, of all chemical classes reported to show causal prophylactic activity in vivo, only the 8-aminoquinolines also display radical cure activity (*27*), suggesting that only a small fraction of the compounds identified in our screen would have similar properties. Nonetheless, it remains to be determined how physiologically distinct a hypnozoite is from an EEF schizont and whether these differences could prevent a drug from acting on both forms. Interestingly, our data show that the known, hypnozoite-targeting compound primaquine acts against the earliest EEFs in our *P. yoelii* cell culture models, suggesting that early acting compounds such as GNF179 may also have similar activity. Nevertheless, as long as these differences are not defined and there are no suitable model systems, the possibility remains that any drug developed with the use of rodent parasite EEF screens may not be efficacious in *P. vivax*. Nonetheless, a drug that acted on EEFs but not hypnozoites, although potentially unsuitable for development, could become a tool for understanding hypnozoite biology. Although the targets of most of the compounds analyzed here remain uncharacterized, we have developed methods that allow us to associate targets and compounds with liver-stage activity, especially if they are also active against blood stages (*10*, *28*, *29*).

References and Notes

1. WHO, World Malaria Report 2010. www.who.int/malaria/world_malaria_report_2010/en/index.html (2010).
2. B. Singh *et al.*, *Lancet* **363**, 1017 (2004).
3. A. Trampuz, M. Jereb, I. Muzlovic, R. M. Prabhu, *Crit. Care* **7**, 315 (2003).
4. WHO, Guidelines for the Treatment of Malaria, www.who.int/malaria/publications/atoz/9789241547925/en/index.html (2011), p. 194.
5. A. W. Sweeney, C. R. B. Blackburn, K. H. Rieckmann, *Am. J. Trop. Med. Hyg.* **71**, 187 (2004).
6. R. J. Cohen, J. R. Sachs, D. J. Wicker, M. E. Conrad, *N. Engl. J. Med.* **279**, 1127 (1968).
7. M. D. Coleman, N. A. Coleman, *Drug Saf.* **14**, 394 (1996).
8. A. O. Talisuna, P. Bloland, U. D'Alessandro, *Clin. Microbiol. Rev.* **17**, 235 (2004).
9. A. Gego *et al.*, *Antimicrob. Agents Chemother.* **50**, 1586 (2006).

10. M. Rottmann *et al.*, *Science* **329**, 1175 (2010).
11. G. J. Crowther *et al.*, *Mol. Biochem. Parasitol.* **175**, 21 (2011).
12. K. Gagaring *et al.*, Novartis-GNF Malaria Box, in *ChEMBL-NTD*, www.ebi.ac.uk/chemblntd (2010).
13. S. F. Yan, H. Asatryan, J. Li, Y. Zhou, *J. Chem. Inf. Model.* **45**, 1784 (2005).
14. P. Wang, M. Read, P. F. Sims, J. E. Hyde, *Mol. Microbiol.* **23**, 979 (1997).
15. P. Wang, N. Nirmalan, Q. Wang, P. F. Sims, J. E. Hyde, *Mol. Biochem. Parasitol.* **135**, 77 (2004).
16. T. Wu *et al.*, *J. Med. Chem.* **54**, 5116 (2011).
17. S. Yalaoui *et al.*, *PLoS Pathog.* **4**, e1000010 (2008).
18. H. J. Painter, J. M. Morrisey, M. W. Mather, A. B. Vaidya, *Nature* **446**, 88 (2007).
19. T.-G. Nam *et al.*, *ACS Chem. Biol.* 110908113621066 (2011).
20. I. Maeda, Y. Kohara, M. Yamamoto, A. Sugimoto, *Curr. Biol.* **11**, 171 (2001).
21. E. A. Winzeler *et al.*, *Science* **285**, 901 (1999).
22. M. C. Jonikas *et al.*, *Science* **323**, 1693 (2009).
23. C. Aurrecoechea *et al.*, *Nucleic Acids Res.* **37**, D539 (2008).
24. D. Mazier, L. Rénia, G. Snounou, *Nat. Rev. Drug Discov.* **8**, 854 (2009).
25. Y. Dong *et al.*, *J. Med. Chem.* **53**, 481 (2010).
26. S. A. Charman *et al.*, *Proc. Natl. Acad. Sci. U.S.A.* **108**, 4400 (2011).
27. D. E. Davidson Jr. *et al.*, *Bull. World Health Organ.* **59**, 463 (1981).
28. E. S. Istvan *et al.*, *Proc. Natl. Acad. Sci. U.S.A.* **108**, 1627 (2011).
29. N. V. Dharia *et al.*, *Genome Biol.* **10**, R21 (2009).
30. D. M. Plouffe *et al.*, *Proc. Natl. Acad. Sci. U.S.A.* **105**, 9059 (2008).

Acknowledgments: We wish to thank I. Sherman for helpful comments on the manuscript, members of the New York University Insectary for providing infected mosquitoes and C. Fischli for *P. berghei* efficacy testing. The whole genome sequencing data has been deposited at the National Center for Biotechnology Information (NCBI) Sequence Read Archive database (http://trace.ncbi.nlm.nih.gov/Traces/sra/sra.cgi?) with the project accession no. SRA045972.1. The microarray data has been deposited at the NCBI Gene Expression Omnibus database (www.ncbi.nlm.nih.gov/geo/) with the accession no. GSE32485. The assay data was deposited at the ChEMBL–Neglected Tropical Disease (ChEMBL-NTD) archive (www.ebi.ac.uk/chemblntd/) with the accession nos. CHEMBL1789904, CHEMBL1789905, and CHEMBL1789906. E.A.W. is supported by the Keck Foundation and by the NIH (grant R01AI090141). S.M. was supported by Deutsche Forschungsgemeinschaft (ME 3528/1-1). Funding for M.C.S.L. and D.A.F. is provided in part by the Medicines for Malaria Venture and the NIH (grant R01 AI079709). We gratefully acknowledge translational research support (WT078285) from the Wellcome Trust and funding from the Medicines for Malaria Venture to the Genomics Institute of the Novartis Research Foundation, the Swiss Tropical and Public Health Institute, and the Novartis Institute for Tropical Diseases. All compounds disclosed are either commercially available from compound vendors (vendor identifications can be sourced from the ChEmbl database), or, if members of the imidazolopiperazine series are required, they will be provided by materials transfer agreement. A materials transfer agreement will be provided by P. Froissard and INSERM-UMR945 for requests for the HepG2-CD81-eGFP cell line.

Supporting Online Material

www.sciencemag.org/cgi/content/full/science.1211936/DC1
Materials and Methods
Tables S1 to S13
Figs. S1 to S5
References (*32*–*61*)

29 July 2011; accepted 6 October 2011
Published online 17 November 2011;
10.1126/science.1211936

Carving at the Nanoscale: Sequential Galvanic Exchange and Kirkendall Growth at Room Temperature

Edgar González,[1,2]* Jordi Arbiol,[3,4] Víctor F. Puntes[1,2,4,5]†

Shape control of inorganic nanocrystals is important for understanding basic size- and shape-dependent scaling laws and is useful in a wide range of applications. With minor modifications in the chemical environment, it is possible to control the reaction and diffusion processes at room temperature, opening up a synthetic route for the production of polymetallic hollow nanoparticles with very different morphology and composition, obtained by the simultaneous or sequential action of galvanic replacement and the Kirkendall effect.

We use molecular reducing agents and coordinating complexes to facilitate combined galvanic exchange and Kirkendall growth at room temperature to produce very unique structures of high complexity, in a context where structure determines properties. These structures, from monodisperse single- and double-walled open nanoboxes to noble metal fullerenes-like nanoparticles (NPs), are produced in a simple manner at room temperature, in the aqueous phase, in high yields, with a large-scalable synthesis (fig. S1).

The production of metallic hollow NPs, either by galvanic replacement (*1*) or by the Kirkendall effect (*2*), requires high temperatures to ensure structures with soft surfaces and well-defined morphology (*3*, *4*). Protocols at lower temperatures would require an increase of the diffusion coefficient to favor mobility of vacancies and jumps of atoms in the crystal and dissolution of the compounds with low solubility formed during the oxidation process. Both of these are important problems because of their influence on the crystallization of metallic surfaces, specifically epitaxial growth (*3*). This is fundamental for the appealing applications of hollow NPs in many areas of science and technology—such as catalysis (*5*), plasmonics (*6*), bioencapsulation (*7*), drug delivery (*8*, *9*), and nanoelectronics (*10*)—where they are excellent benchworks. The interest in developing this kind of nanostructures continues to today, as reflected in more recent literature (*11*–*16*).

By using silver as template; polyvinylpyrrolidone (PVP) as surfactant; cetyl trimethylammonium bromide (CTAB) as surfactant and complexing agent; gold, palladium, and platinum as oxidizing agents; and ascorbic acid as reducing agent; nanoparticles with different levels of structural hierarchy were easily obtained at room temperature. In the presence of CTAB, ascorbic acid reduces $AuCl_4^-$ to $AuCl_2^-$ (*17*), decreasing its lability and allowing Kirkendall effect to take place. Furthermore, it solubilizes AgBr and AgCl formed upon oxidation of silver (*18*) (also fig. S2). A detailed explanation on the synthetic procedures is given in the Materials and Methods section of the supporting online material (SOM).

As an example, Fig. 1 shows concentric double-walled nanoboxes. When the reaction begins, oxidation of silver provides one electron to reduce one gold ion. Because gold and silver have the same face-centered cubic (fcc) structure and about equal lattice constants, gold atoms are epitaxially deposited onto the silver surface as a thin layer (Fig. 1A2). The covering of Ag with Au protects Ag from oxidation. As the relative area of the electrodes increases, corrosion becomes progressively stronger at the uncovered areas, which leads to the formation of pinholes, from which the silver cube is emptied. A galvanic reaction follows between the Ag inner electrode and the Au outer one, in which the pitting site serves as the anode where the silver is oxidized and its electrons are stripped. The released electrons can easily migrate to the surface of the nanocube and are captured by $AuCl^-_2$ ions to generate gold atoms that preferentially nucleate and grow on the surface of the template (Fig. 1A4). The dissolution of Ag^+ ions increases the local concentrations of Br^- and Cl^-, favoring pit growth by autocatalytic processes (*19*). As the

[1]Institut Català de Nanotecnologia (ICN), Campus UAB, 08193 Bellaterra, Spain. [2]Universitat Autònoma de Barcelona (UAB), Campus UAB, 08193 Bellaterra, Spain. [3]Institut de Ciència de Materials de Barcelona (ICMAB-CSIC), Campus UAB, 08193 Bellaterra, Spain. [4]Institució Catalana de Recerca i Estudis Avançats (ICREA), Passeig Lluís Companys, 23, 08010 Barcelona, Spain. [5]Centre d'Investigacions en Nanociència i Nanotecnologia CIN2 (ICN-CSIC), Campus UAB, 08193 Bellaterra, Spain.

*Present address: Sección de Nanociencia y Nanotecnología, Instituto Geofísico, Pontificia Universidad Javeriana, 110231 Bogotá, Colombia.

†To whom correspondence should be addressed. E-mail: victor.puntes@icn.cat